

Energy harvesting from cavity flow oscillations

Varun Thangamani  and Foo Ngai Kok

Journal of Intelligent Material Systems
and Structures
1–19

© The Author(s) 2021



Article reuse guidelines:

sagepub.com/journals-permissions

DOI: 10.1177/1045389X211014949

journals.sagepub.com/home/jim



Abstract

This study investigates the energy harvesting prospects of self-sustained flow oscillations emanating from grazing flow over a rectangular cavity by employing experimental and computational methods. Two cavity geometries with length-to-depth ratios of 2 and 3, exposed to an incoming flow of 30 m/s, were selected for the purpose. The power spectral density of the baseline cavity flows showed the presence of high-amplitude peaks whose frequencies agreed to those estimated from Rossiter's feedback model. For energy harvesting, a piezoelectric beam was placed perpendicular to the aft wall and its natural frequency tuned to match closely with the dominant frequencies of the cavity flow oscillations. From the experiments, an average and maximum instantaneous power of 21.11 and 284.18 μW was recorded for the cavity with $L/D = 2$ whereas for the cavity with $L/D = 3$ the corresponding values were 32.16 and 403.46 μW respectively. Time-frequency analysis showed the forcing of the beam at the cavity oscillation frequency and the substantial increase in the amplitude of beam vibrations when this frequency was close to the natural frequency of the beam.

Keywords

Cavity flow oscillations, energy harvesting, piezoelectricity

1. Introduction

The quest to harness energy from surrounding natural resources can be dated back centuries. However, in the recent decade, with the advent of micro and nanoscale electronic sensors and systems, the scope has now expanded to conform to these scales as well. Finding power sources at these scales, especially cost-free, from the ambience where energy can be scavenged and harvested, have gained traction. The field has been made all the more conducive and pertinent owing to the flourish of technologies such as the Internet of Things (IoT), wireless sensor networks, MEMS-based portable devices and monitoring systems. Powering such micro-electronic systems using a renewable source of energy would be a win-win situation for both society as well as the environment. They reduce wastage, maintenance cost and pollution of the environment.

Pertinent to micro-scale power plants, recent research indicates that energy harvesting from fluid flows is a promising technique with broad applications (Hamlehdar et al., 2019). While conventional methods like turbines are suitable for large scale power generation, they are vastly inefficient, complicated and expensive at small scales (Mitcheson et al., 2008). The influence of damping forces and coil turns achievable at the MEMS scale makes turbines and other

electromagnetic harvesters largely impractical in these applications. The harnessing methods employed to extract energy from fluid flow at these scales are largely vibrations-based, wherein energy from the flow is converted into mechanical vibrations of a transducer which further transforms them into electrical energy. Some of the most widely used transducers in research are based on electromagnetic and piezoelectric principles. Piezoelectric harvesters are particularly well-suited due to their scalability to miniature applications, low-voltage operation and easier tunability to high frequencies for resonant operations. Energy harvesting oscillators using this principle capture the structural vibrations caused as a result of flow-structure interaction or use the unsteady flow field created owing to a body placed in the flow. Energy harvesting from flutter and galloping belong to the former method while Vortex-Induced Vibrations belong to the latter.

In flutter-based energy harvesting, the vibration of energy harvesters is caused due to aeroelastic

University of Southampton Malaysia, Iskandar Puteri, Johor, Malaysia

Corresponding author:

Varun Thangamani, University of Southampton Malaysia, No. 3 Persiaran Canselor I, Kota Ilmu Educity, Iskandar Puteri, Johor 79200, Malaysia.
Email: V.Thangamani@soton.ac.uk

instabilities caused in a body due to the incoming airflow. The flow excites two or more modes of vibration in the body (typically a wing) that gets coupled and extract energy from the incoming flow. However, the airflow velocity has to attain a certain threshold value to activate the self-excited vibrations. Below the threshold value, the vibrations are damped by the wing material. When the flow velocity is increased far above the threshold value, large limit cycle oscillations occur due to aerodynamic and elastic non-linearities (Abdelkefi, 2016). Bryant and Garcia (2011) used a linear analytical model to study the onset of flutter vibrations and to study the frequency and wind speed when they start occurring. At higher wind speeds, they used a semi-empirical non-linear model to simulate the limit cycle oscillations using empirical coefficients from wind tunnel testing. Dunnmon et al. (2011) proposed a theoretical non-linear model for the self-excited limit cycle oscillations for an aeroelastic energy harvester. Concurrent experimental results on a NACA0015 airfoil of 550 mm span and 101 mm chord length produced a root mean square power of 2.5 mW at a wind velocity of 27 m/s. Using the apparatus, they were able to access a fifth of the flow energy for harvesting purpose.

In the galloping method, a bluff body like a prism is placed in a flow to excite aeroelastic instabilities above a cut-in velocity. The oscillations are of large amplitude and take place in a transverse direction to the flow. For galloping to occur, the aerodynamic lift coefficient derivative is required to be negative (Hartog, 1985). Sirohi and Mahadik (2011) conducted a successful attempt at harnessing energy using a cantilever beam with a piezoelectric patch attached to a triangular prism exposed transversely to the wind. They were able to harness a maximum power of 53 mW from the galloping motions of the structure at a wind velocity of 11.6 mph. They also supplemented their results with a detailed analytical model to deduce the voltage generated in their device across parameters like wind velocity, load resistance and beam geometry. Bibo et al. (2015) developed an aero-electromechanical model to describe the non-linear behaviour of an energy harvester that is under a combined galloping and base excitations.

Safety considerations become essential for flutter and galloping methods at higher wind speeds since the amplitude of oscillations can get inordinate. Another disadvantage with flutter and galloping is that they need sizeable structures to capture the energy which may make them difficult to adapt for internal flows. In Vortex-Induced Vibrations (VIV), the unsteady vortex shedding by a bluff body is used to induce a periodic fluid dynamic force on a structure, resulting in its oscillations. When coupled to an energy harvester, this oscillating motion of the structure is converted to electric energy. Wen et al. (2014) utilized a VIV based energy harvester using a cuboidal bluff body and a

piezoelectric cantilever beam placed in the wake region. They recorded power of 1 μ W at an airflow velocity of 2 m/s, corresponding to an eigen frequency of 5 Hz for the cantilever beam. Allen and Smits (2001) used a flat plate oriented normally to the incoming flow to move a flexible PVDF (polyvinylidene fluoride) cantilever in a water tunnel.

Apart from the above, there have also been studies aimed at harvesting energy from flow-induced acoustic resonance. Matova et al. (2011) used air oscillations in a Helmholtz resonator to vibrate a piezoelectric energy harvester. They tuned the frequency of the Helmholtz resonator to match with that of the piezoelectric diaphragm they used in the bottom of the resonator and were able to harvest 2 μ W at an airflow velocity of 13 m/s. Zou et al. (2015) used a fluidic 1 mm diameter air jet to induce acoustic resonance inside a 10 mm long pipe resonator where a PZT-5H piezoelectric transducer was embedded. The harvester yielded a power of 85 mW relative to an airflow velocity of 159 m/s. Akaydin et al. (2010b) placed short PVDF piezoelectric cantilever beams in the wake region of a cylinder at Reynolds number range 10,000–21,000. When resonance occurred at $Re = 14,800$, maximum power of 4 μ W was obtained when the beam was kept at a downstream distance twice the cylinder diameter (Akaydin et al. 2010a). Another exciting development happened with exploring turbulence-induced excitation (Akaydin et al., 2010a). Goushcha et al. (2015) explored the feasibility of energy harvesting from a turbulent boundary layer. They placed PVDF piezoelectric beams on turbulent boundary layers where Re_θ varied between 2000 and 7500. They studied parameters like location, orientation, turbulence intensity and piezoelectric beam material on the power generated. Their flow visualizations revealed impingement of turbulent vortical structures on the beam. However, the randomness of the time and length scales made achieving resonance challenging. Power output increased with velocity and proximity to the wall where turbulence intensity is high. The maximum power that had been measured was 0.06 μ W.

When it comes to harvesting energy from unsteady flow fields, the potential of cavity flow oscillations as a possible candidate is worth exploring. Research into cavity flows goes back as early as the 1950s. Grazing flow over certain rectangular cavity cut-outs is known to generate self-sustaining oscillations. Rossiter (1964) was one of the first investigators to propose a physical model that attributed to the generation of tones. According to his model, vortical disturbances shed from the cavity leading edge convect downstream and impinge at the aft wall. This impingement creates a transient high-pressure zone in front of the aft wall that generates an acoustic pressure wave that propagates in the upstream direction. This acoustic wave acts as feedback and further induces vortical disturbances at the cavity leading edge, which convects downstream to

continue the cycle. While the vortical convection has been debated since they are not observed in all flow conditions, the presence of the acoustic feedback between the front and aft wall has been well established and is widely accepted. Heller and Bliss (1975) constructed an analytical model where they assumed the shear layer oscillations as flapping motions that periodically adds and removes mass into the cavity near the trailing edge, thus creating pressure fluctuation there. Cavity flow oscillations are largely undesirable, and several methods have been investigated to control them (Cattafesta et al., 2003; Saddington et al., 2016b; Thangamani and Kurian, 2013).

The various cavity flow control methods aim at disrupting one or more components of the feedback cycle that is responsible for the oscillations (Saddington et al., 2016a; Thangamani et al., 2014; Zhang et al., 1998). While detrimental otherwise, the self-sustained oscillations have the potential to power micropowered devices if harvested efficiently. There is a semi-empirical relation governing the frequency of oscillations, and this can be used to tune the harvester to lock in with the flow oscillations in order to derive maximum power. These concepts are explored in this work, through experiments and computations, and the potential of cavity flow oscillations for energy harvesting has been studied. The results show promise and justify further investigations. Possessing a simple geometry, a cavity flow-based energy harvesting device can be easily envisaged in numerous scenarios such as aircraft, automobiles, pipelines and even rivers for powering sensors.

In this work, a preliminary study to investigate the application of cavity flow oscillations for micro-energy harvesting is carried out. For this, a rectangular cavity of specific geometrical parameters that are expected to generate high-amplitude tones had been selected and tested for its unsteady pressure environment. A piezoelectric cantilever beam is fixed inside the cavity and tuned to lock in with the cavity oscillation frequencies and the power generated by the harvester is measured across a single resistor load. Due to the complex and transient nature of the flow, computer simulations were also carried out for one of the baseline cavity flow case to understand the flow features that give rise to the unsteadiness.

2. Experimental details

The experiments were carried out at the Thermofluids lab of the University of Southampton Malaysia. The chief aim behind the experimental design was to construct a small, simple apparatus that is capable of generating micro-wattage power by harnessing cavity-generated flow oscillations. For this, two small bespoke test sections, each embedded with a different

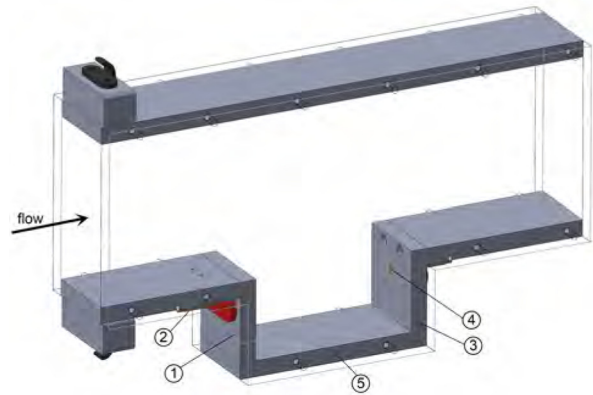


Figure 1. Test Section embedded with cavity. Numbered components show the (1) front wall, (2) front wall microphone, (3) aft wall, (4) aft wall microphone and (5) cavity floor.

rectangular cavity on one side of the wall was fabricated using transparent acrylic material (as shown in Figure 1). The test section was fitted to the air outlet of a small-scale wind tunnel manufactured by TecEquipment®, called as AF10. The AF10 can deliver a uniform airflow of velocity up to 30 m/s. The whole test section is 310 mm long and has an inlet of dimensions 100 mm × 50 mm. Air flow to the test section is regulated by a control valve before letting into a settling chamber. From the settling chamber, the air is accelerated through a convergent nozzle to a rectangular exit. Some minor components of the test section, like clamps and microphone fixtures, were 3D printed. The objectives of the experiments were to study the flow unsteadiness created due to the presence of the cavity, deduce the location and configuration to fit a piezoelectric beam inside the cavity and then measure the power generated by a piezoelectric energy harvester.

The unsteadiness created inside a cavity environment is largely dependent on the length-to-depth (L/D) ratio of the cavity (Tracy and Plentovich, 1993). Cavities with $L/D < 10$ are classified as open cavities whereas those with $L/D > 10$ as closed cavities. However, this demarcation is also dependent on the Mach number of the incoming flow. In open cavities, the shear layer separating from the leading edge of the cavity bridges across the cavity length without touching the cavity floor whereas in closed cavities the shear layer touches the floor. There is also a transitional phase (transitional cavities) between the two. Open cavities have been known to exhibit high-amplitude tones due to the presence of an effective feedback cycle. Oscillations are generally absent in closed cavities since the shear layer does not directly impinge on the aft wall to initiate the feedback cycle. Hence for the current studies, two rectangular cavity geometries were selected – the first with an $L/D = 2$ and the second with $L/D = 3$. Both the

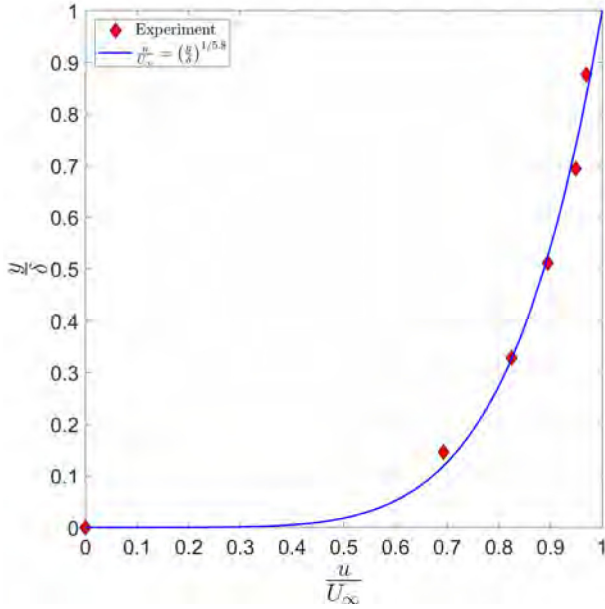


Figure 2. Boundary layer profile measured at $(\frac{x}{L}, \frac{y}{D}, \frac{z}{W}) = (0, 0, 0)$.

geometries clearly belong to the open cavity flow classification and can be expected to generate significant flow oscillations. For brevity, the test section embedded with the cavity of $L/D = 2$ will be referred to as CM2 (Cavity Model with $L/D = 2$) and one with $L/D = 3$ as CM3. The cavity dimensions for CM2 is $L \times W \times D = 100 \text{ mm} \times 50 \text{ mm} \times 50 \text{ mm}$ whereas of that of CM3 is $150 \text{ mm} \times 50 \text{ mm} \times 50 \text{ mm}$. The length-to-width (L/W) ratio affects the three-dimensionality and tonal amplitudes associated with the flow. The L/W ratio of CM2 and CM3 is 2 and 3, respectively. In his studies on the effect of cavity width, Ahuja and Mendoza (1995) found that the sound power levels of the cavity increased with an increase in cavity width, keeping other factors constant. However, the tonal frequencies remained unaffected with the change in cavity width. Hence, if other parameters are kept the same, an open cavity with a low value of L/W is desirable from an energy harvesting perspective.

The origin for the flow coordinate system in this study is fixed at the midpoint of the cavity leading edge. The incoming flow direction is treated as the x -axis and the cavity span direction as the z -axis (Figure 6). The incoming flow speed for the experiments was set to 30 m/s, and the velocity was measured using a pitot tube and pressure tap located at the test section inlet. The boundary layer at the cavity leading edge was measured using a boundary layer probe mounted on a screw gauge and the thickness based on 99% freestream velocity, $\delta_{0.99}$, was found to be 1.37 mm. The displacement thickness and momentum thickness estimated from velocity profile measurements were $\delta^* = 0.26 \text{ mm}$ and $\theta = 0.13 \text{ mm}$, respectively. The values of δ^* and θ

Table 1. Properties of the piezoelectric material (PZT-5H) used in the energy harvester.

Property	Symbol	Value
Piezoelectric-charge coefficients	d_{31}	$-320 \times 10^{-12} \text{ C/N}$
	d_{33}	$650 \times 10^{-12} \text{ C/N}$
Piezoelectric-voltage coefficients	g_{31}	$-9.5 \times 10^{-3} \text{ Vm/N}$
	g_{33}	$19 \times 10^{-3} \text{ Vm/N}$
Coupling coefficients	k_{31}	0.43
	k_{33}	0.75
Density	ρ_b	7870 kg/m^3
Young's modulus	Y_{11}	$7 \times 10^{10} \text{ N/m}^2$
	Y_{33}	$11 \times 10^{10} \text{ N/m}^2$

yields the shape factor for the boundary layer, $H = 2$, indicating its tendency to separate at the lip owing to the adverse pressure gradient present there. A power-law profile given by equation (1) was found to describe the obtained profile well.

$$\frac{u}{U_\infty} = \left(\frac{y}{\delta}\right)^{1/n} \quad (1)$$

For the current case, $n = 5.8$ was found to be the best fit for the boundary layer profile measured (Figure 2). Based on the estimated displacement thickness value, the blockage to the flow at the transverse plane at cavity leading edge, calculated as $\frac{\delta^* P_i}{A_i}$, is 1.56%, where P_i and A_i are the test section inlet perimeter and cross-sectional area respectively.

For energy harvesting, a single-layered piezoelectric beam bender, S128-H5FR-1107YB, commercially manufactured by Midé was used. The piezoceramic material used in the beam is PZT-5H sandwiched between copper electrodes and a packaging material FR4. The whole beam weighs 2 g and is suited for harnessing vibrations at high frequencies up to 660 Hz. The various properties of the piezoelectric material are given in Table 1. The beam measured $53 \text{ mm} \times 20.8 \text{ mm} \times 0.71 \text{ mm}$ in size and was fixed at one end to be used as a vibrating cantilever. For energy harvesting, the beam was located perpendicular to the cavity wall, as shown in Figure 3. The reasoning and effect of placing the beam at the aft wall and front wall have been discussed in subsequent sections. The piezoelectric beam was mounted perpendicular to the aft wall through a narrow slit of 1.2 mm thickness. A clamp (shown in Figure 4), screwed on to a 3D printed fixture, was used to install and control the vibrating length of the piezoelectric beam.

The fluctuating pressure measurements were made using PCB manufactured 130F21 model pre-polarized microphones. The 130F21 model is an Integrated-Circuit Piezoelectric (ICP[®]) microphone that has a high

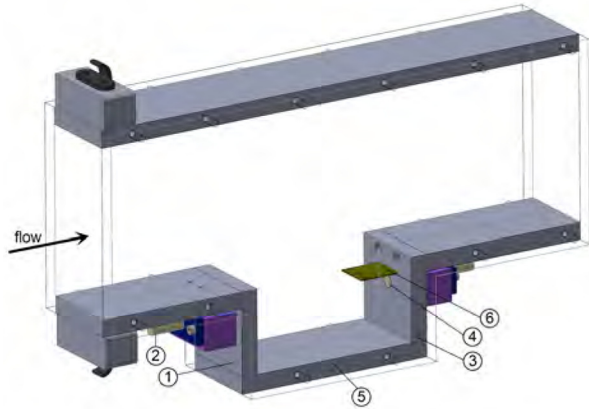


Figure 3. Test section with piezoelectric beam located at aft wall. Numbered components show the (1) front wall, (2) front wall microphone, (3) aft wall, (4) aft wall microphone, (5) cavity floor and (6) piezoelectric beam.

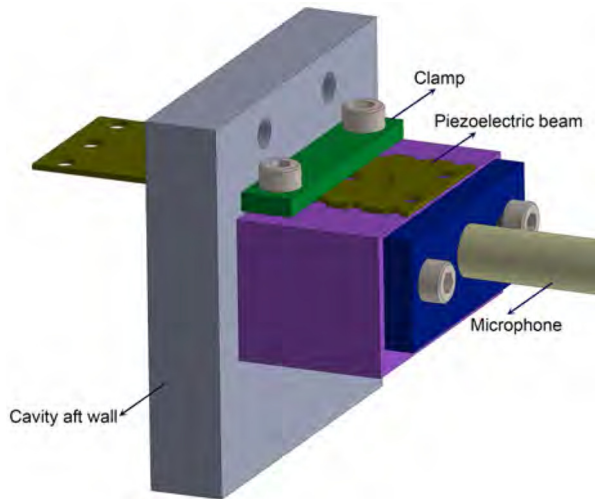


Figure 4. Detailed view of piezoelectric beam installed at aft wall.

sensitivity of 45 mV/Pa and is built with an integrated preamplifier. They have a diameter of 1/4" and were flush-mounted on the cavity surface (Figure 5). Three such microphones were used for both the models CM2 and CM3. They were placed at locations $(x/L, y/D, z/W) = (0, -0.42, 0), (0.5, -1, 0)$ and $(1, -0.42, 0)$. This enables comparison of the fluctuating pressure levels at the front wall, cavity floor and aft wall, respectively. The signals obtained from the microphones and energy harvester were acquired and recorded using a National Instruments data acquisition module NI USB-4431. The NI USB-4431 has a 24-bit resolution and is capable of acquiring signals at a sampling rate of up to 102.4 kHz. It is specifically designed for sound and vibration measurements and thus well suited to the



Figure 5. Test section assembly attached to flow bench (flow direction is vertically downwards). Numbered components show the (1) front wall, (2) front wall microphone, (3) cavity, (4) aft wall microphone, (5) rectangular test section with embedded cavity, (6) piezoelectric beam, (7) settling chamber and (8) converging nozzle.

current study. The analog-to-digital conversion and signal conditioning are also carried out by the NI USB-4431, which was interfaced and controlled through LabVIEW software. For any given test, the signals from three microphones and the energy harvester, if present, were acquired simultaneously. The experiments were found to be repeatable, and the frequencies of the dominant mode of cavity oscillations were found to be invariable between different runs. To quantify Type A uncertainty (Kirkup and Frenkel, 2006) in the measurement of amplitude, ten different runs were carried out under the same test conditions, and the standard uncertainty based on n observations and a standard deviation σ , for a 95% confidence interval, is calculated as

$$\epsilon_{0.95} = \pm 1.96 \frac{\sigma}{\sqrt{n}} \quad (2)$$

The maximum standard uncertainty in amplitude seen in the power spectral density plots, calculated using equation (2), for any of the first three cavity modes of oscillation was $\pm 0.71 \text{ Pa}^2/\text{Hz}$.

3. Computational details

Numerical simulations were carried out to provide insights into the unsteady flow structures that develop in the cavity. The main motive was to understand the fluctuating environment inside the baseline cavity so as to use this information to arrive upon a rational location to place the piezoelectric beam inside the cavity. In order to achieve this, only the CM3 was simulated since it showed higher levels of unsteadiness during the

experiments. The simulation was performed using ANSYS Fluent 19.1 based on the cell-centred finite volume discretization method. The incompressible large-eddy simulation (LES) technique was adopted in the present study to predict the pressure fluctuations inside the cavity region. The filtered mass and momentum transport equations are given by:

$$\frac{\partial u'_i}{\partial x_i} = 0 \quad (3)$$

$$\frac{\partial u'_i}{\partial t} + \frac{\partial u'_i u'_j}{\partial t} = \frac{\partial}{\partial x} \nu \left(\frac{\partial u'_i}{\partial x_j} + \frac{\partial u'_j}{\partial x_i} \right) - \frac{1}{\rho} \frac{\partial p'}{\partial x_i} \quad (4)$$

$$\tau_{ij} = u'_i u'_j - u'_i u'_j \quad (5)$$

where u_i is the i th component of the velocity vector, p is the pressure, ν is the kinematic viscosity and τ_{ij} is the subgrid-scale (SGS) stress tensor. The unresolved subgrid-scale (SGS) stresses are modelled using Smagorinsky model (Smagorinsky, 1963) based on the Boussinesq approximation of subgrid viscosity:

$$\tau_{ij} = \frac{1}{3} \tau_{kk} \delta_{ij} - 2\nu_{SGS} S'_{ij} \quad (6)$$

where ν_{SGS} is the subgrid scale turbulent viscosity and S'_{ij} is the subgrid scale shear strain tensor which is given by

$$S'_{ij} = \frac{1}{2} \left(\frac{\partial u'_i}{\partial x_j} + \frac{\partial u'_j}{\partial x_i} \right) \quad (7)$$

and

$$\nu_{SGS} = (C_S \Delta)^2 \sqrt{S'_{ij} S'_{ij}} \quad (8)$$

where C_S is the Smagorinsky constant which is set to 0.1, and Δ is the filter width.

The filtered Navier-Stokes equations were solved using the pressure-based solver. The Semi-Implicit Method for Pressure-Linked Equations (SIMPLE) scheme was employed in the solver for pressure and velocity coupling. In order to reduce the effect of numerical diffusion in the simulation, the convective fluxes were discretized using second-order-accurate bounded central differencing scheme. The discretized transport equations were advanced in time by an iterative time-advancement scheme with twenty inner iterations. A time-step size of 10^{-5} s, corresponding to a non-dimensional time-step $\frac{\Delta t U_\infty}{L}$ of 1.9×10^{-3} , was applied for the present simulation. The corresponding CFL to the chosen time-step is found to be less than 1.5. The LES data were collected after about seven flow-through times which was found to be long enough for the statistically steady solution to be reached. The statistical data were collected over an additional 63 flow-through times.

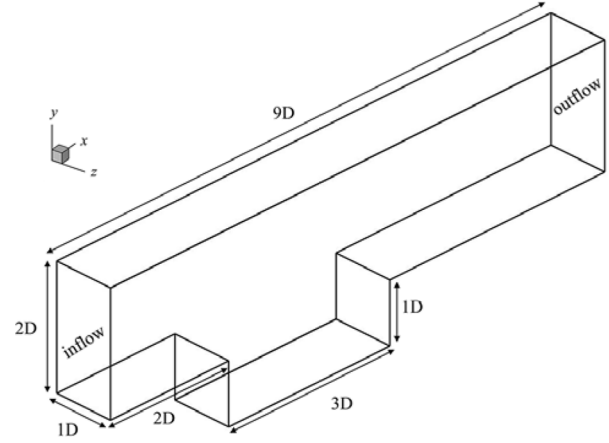


Figure 6. Geometry of the computational domain.

The geometry of the computation domain is shown in Figure 6. The dimensions of the cavity are the same as the experimental model which has a length-to-depth ratio of 3, a width of 1D and a length of 0.15 m. For the rectangular channel above the cavity, the height and the width of the rectangular channel are equal to the experimental model. The inflow boundary is located 2D away from the upstream wall of the cavity whereas the outflow boundary is 4D away from the downstream wall of the cavity. The origin of the coordinate system is located at the centre of the leading edge of the cavity. The computational domain consists of 1.6 million cells ($250 \times 80 \times 80$) inside the cavity region and 3.36 million cells ($350 \times 120 \times 80$) inside the rectangular channel above the cavity. A total of 30 cells were clustered in a 0.1D space region near the walls of the rectangular channel with a stretching ratio of 1.02. The first cell is 0.0002D away from all the wall, corresponding to a $y^+ < 1$. Another 40 cells were distributed uniformly in the traverse direction from $y = 0.1-0.3D$ to increase the resolution of the free shear layer.

The inflow velocity profile was obtained from a separate Reynolds averaged Navier-Stokes (RANS) simulation of a rectangular channel with a cross-section area identical to the experimental model and a length of 4D. In this simulation, a uniform velocity profile with a relatively low turbulent intensity of 0.5% was assigned at the inlet. The freestream velocity was maintained the same as that of experiments. The velocity profile obtained from the RANS simulation was then applied at the inflow boundary of the cavity model. At the outflow boundary of the cavity model, a traction-free boundary condition was assigned. All the walls were treated as no-slip surfaces.

4. Grid resolution effects

Before comparing the numerical results with the experimental data, the effect of grid resolution of the

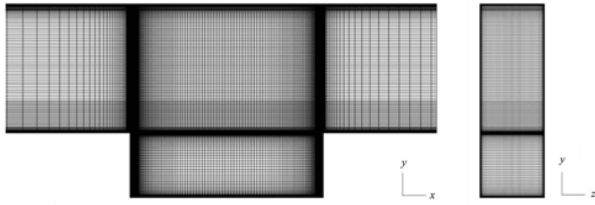


Figure 7. View of the grid distribution in the x - y plane (a) and the y - z plane (b) of the computation domain.

computational model was examined. Two different computational models were generated to evaluate the influence of spanwise and streamwise grid resolutions. The first model consists of about 0.5 million cells ($150 \times 80 \times 40$) inside the cavity and 1.02 million cells ($350 \times 85 \times 40$) in the rectangular channel. The mesh is referred to as the coarse mesh. The second model consists of 1.6 million cells ($250 \times 80 \times 80$) inside the cavity and 3.36 million cells ($350 \times 120 \times 80$) in the rectangular channel and is referred to as the fine mesh. The computational grid on the symmetry plane and the cross-section of the fine mesh model is illustrated in Figure 7. For both models, the cell sizes at the near walls of the cavity and rectangular channel were kept the same as described in the previous section. The statistical data were collected with a physical sampling time of 0.6 s, after a relaxation time of 0.11 s (approximately seven flow-through times) which is long enough for the statistically steady solution to be reached.

Figure 8 shows the profiles of the normalized mean streamwise velocity component, \bar{u} , at four different locations ($x/D = 0.6, 1.2, 1.8$ and 2.4) along the cavity region. The results show that increasing the grid resolution in the streamwise and the spanwise directions from 150 to 250 and from 40 to 80, respectively, has no major influence on the mean velocity profiles. The coarse mesh, in general, exhibits a lower magnitude in the rectangular channel and a slightly higher peak in the cavity region. However, at all the locations considered, the profiles are generally in good agreement with the fine mesh solutions. The corresponding Reynolds stresses $u'u'$, $v'v'$ and $u'v'$ are also presented in Figure 8. All stresses are normalized by the freestream velocity U_∞ . The results from the coarse mesh, in general, are in good agreement with that of the fine mesh. A major difference is observed at the lower upstream vicinity of the cavity. At $x/D = 1.2$, the increase of grid resolution in the fine mesh model generally reduces the overall stress levels at the near-wall region.

5. Results and discussion

5.1. Baseline cases

To effectively harness the oscillatory energy of the flow, it is imperative to understand the nature of pressure

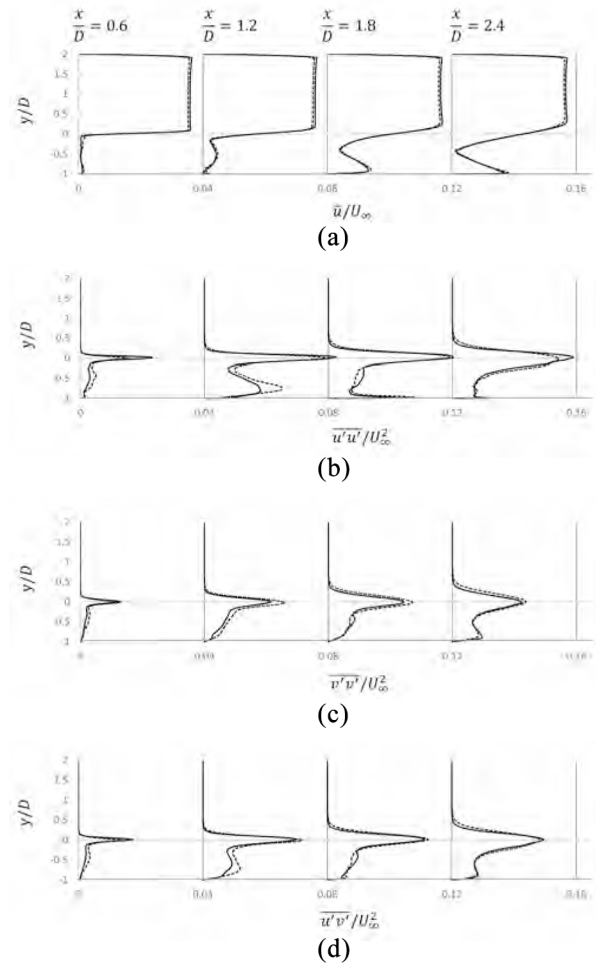


Figure 8. Comparison of the normalized mean streamwise velocity u (a) and the Reynolds stresses profiles $u'u'$ (b), $v'v'$ (c) and $u'v'$ (d) at four streamwise locations of central plane of the cavity: dashed line = coarse mesh, solid line = fine mesh. Offsets of $+0.04$, $+0.08$ and $+0.12$ are introduced to $x/D = 1.2, 1.8$ and 2.4 for clarity purposes.

unsteadiness and flow pattern generated in the cavity environment. Hence, the results of the clean cavity without any energy harvester, also known as the baseline cavity, are discussed first. The frequencies of flow oscillations were deduced experimentally from acoustic pressure data obtained using the microphones flush-mounted on the cavity front wall, floor and aft wall. The signals from the three microphones were acquired simultaneously at a sampling rate of 32,768 samples per second. For a given tunnel run, a total of 327,680 samples were collected over 10 s. The data obtained were used to plot the power spectral density using Welch's method. To evaluate the spectrum, the 327,680 samples that were obtained per channel were segmented to 8192-point Fast Fourier Transforms (FFT) with a 50% overlap using a Hamming window, yielding a frequency resolution of 4 Hz. To get an accurate shape of the frequency spectrum for the cavity, spectral data from ten different tunnel runs were ensemble-averaged and the

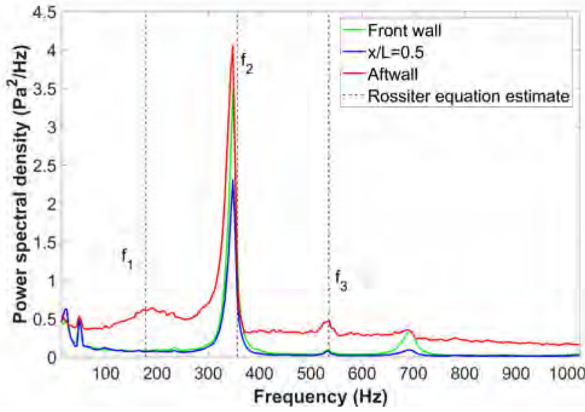


Figure 9. Baseline power spectral density for CM2 shown along with frequencies estimated using equation (9).

spectra thus obtained for CM2 and CM3 have been shown in Figures 9 and 10 respectively.

From the power spectral density plots of CM2 and CM3, high amplitude peaks can be discerned at specific frequencies. The first three modes of cavity flow oscillation will be hereafter denoted as f_1 , f_2 and f_3 respectively. The higher modes above f_3 are feeble and barely distinguishable from the noise floor of the spectrum. For CM2, f_2 is the only dominant mode of oscillation in the baseline case. However, for CM3, two modes have very high amplitudes viz. f_2 and f_3 . It is common for the first three to four modes to account for most of the oscillation energy. It can be noticed that the noise levels for the front wall and floor ($x/L = 0.5$) are lower when compared to the aft wall. This is in line with expectation since the aft wall is exposed to the shear layer dipping and partly stagnating in front of it during an oscillation cycle, thus leading to very high pressure-fluctuations and noise levels.

Rossiter used an empirical formula given by equation (9) to estimate the cavity frequencies by accounting for the various elements in his proposed model.

$$\frac{f_m L}{U_\infty} = \frac{m - \alpha}{M_\infty + \frac{1}{k}} \quad (9)$$

In the above equation, f_m is the frequency of cavity oscillation of the m^{th} mode, L is the length of the cavity, α is an empirical constant to account for the time lag between the shear layer interaction with the aft wall and the creation of acoustic wave from there, U_∞ is the freestream velocity, M_∞ is the flow Mach number and k is the ratio of vortex convection velocity to freestream velocity. Although Rossiter used α and k to be 0.25 and 0.57 as the best fit to the data he obtained from his experiments, many researchers over the years have used various values for the two empirical constants. Several works have noted that for a low Mach number, as in the current case, the value of α can be set to 0 since the

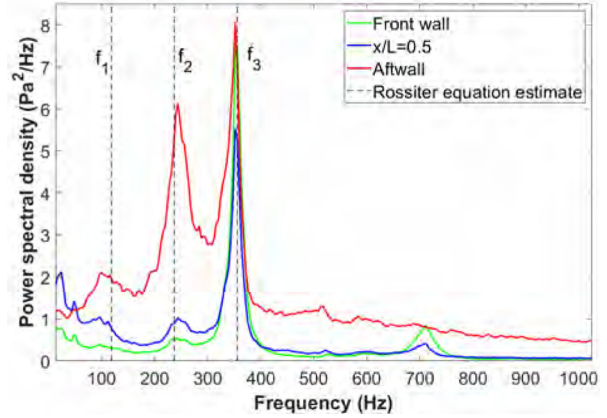


Figure 10. Baseline power spectral density for CM3 shown along with frequencies estimated using equation (9).

time lag between the events of shear layer impingement and acoustic wave creation is negligible (Chatellier et al., 2004; Ma et al., 2009; Verdugo et al., 2012). Keeping $\alpha = 0$ and $k = 0.63$ gave the best fit for the experimental data obtained for the current case. This would imply that the frequencies estimated using Rossiter's model would be harmonics given by $f_m = m f_1$. The cavity frequencies estimated from equation (9) has also been shown concurrently with the power spectral density on Figures 9 and 10. It can be noticed that the frequencies obtained from the experiments are in good agreement with Rossiter's equation and lies within 2.8% variation. It can thus be inferred that Rossiter's feedback model is responsible for the generation of the high-amplitude frequencies seen in the frequency spectra. Of the two cavities, the flow oscillations of CM3 are comparatively severe than CM2 and can be expected to produce better results for energy harvesting purpose.

5.2 Computational results

To decide upon the location and manner for placing the piezoelectric beam, an understanding of the flow field inside the cavity is essential. For this, computational simulation results have been utilized to visualize the flow. The fluctuating pressure data at corresponding locations were used to validate the computational results, and the agreement between experiments and CFD was found to be fair. Figures 11 and 12 show the comparison between the time series of fluctuating pressure, p' ($p' = p_i - \bar{p}$, where p_i is the instantaneous pressure and \bar{p} is the time-averaged pressure), and the power spectral density obtained for CM3 at the same aft wall location. While the frequencies of the first three modes obtained using experimental measurements were 116 Hz, 244 Hz and 352 Hz, the corresponding frequencies obtained using CFD were 92 Hz, 244 Hz and 336 Hz. This indicates a difference of 20.6%, 0% and

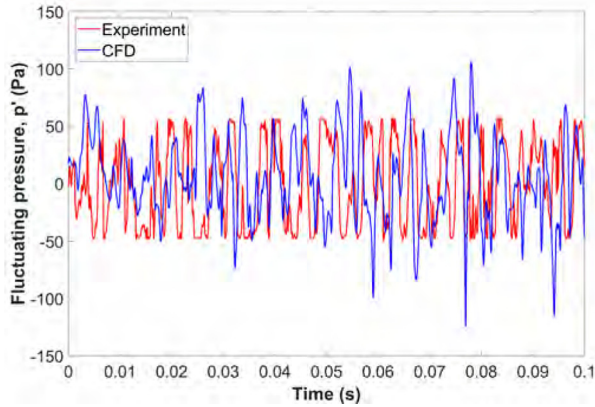


Figure 11. Comparison of power spectral density at aft wall between measurement and CFD (CM3).

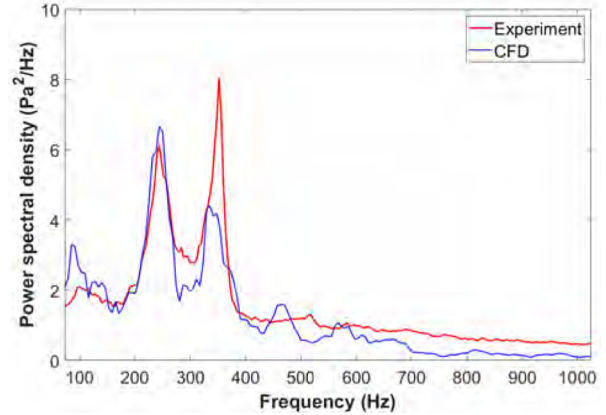


Figure 12. Comparison of fluctuating pressure at aft wall between measurement and CFD (CM3).

4.6% for f_1 , f_2 and f_3 respectively. The comparatively higher deviation seen for f_1 , which is the weakest mode, is due to the absence of a prominent frequency peak in this mode as can be seen from Figure 12 and the peak is spread over a wider band of frequencies. The maximum difference in amplitude between the CFD and experiments is $4.4 \text{ Pa}^2/\text{Hz}$ for f_3 . The discrepancies present between the experimental and simulation results can be attributed to the absence of realistic turbulent structures at the inlet. In this study, the LES was performed using a less expensive inflow condition in which the inflow turbulent data were obtained from a separate RANS simulation. The lack of realistic turbulent fluctuations at the inflow boundary condition may lead to different energy levels in the separated shear layer downstream of the channel resulting in slight differences. To obtain a more satisfactory prediction for the unsteady flow field in the cavity, the shear layer above the cavity must be resolved accurately, and this can be achieved by imposing a realistic turbulent velocity profile at the upstream edge of the cavity (Chang et al., 2006; Larcheveque et al., 2007).

To extract the oscillatory energy of the flow, the piezoelectric beam has to be placed at a location where the pressure forces acting on it are high and periodic, subjecting it to vibrations with high tip-deflections. Figures 13 and 14 show the RMS contour plot of the fluctuating pressure and velocity respectively at the midplane. Contours of high fluctuations are concentrated towards the aft wall lip, making it an attractive position to place the beam. It was decided to locate the transducer perpendicularly to the aft wall at a distance of $0.22D$ down from the lip. This would utilize, without breaking up, the entire high fluctuating ‘red’ region shown in Figure 13.

While Figures 13 and 14 give the RMS quantities, from an instantaneous and temporal perspective, the free shear layer spanning the cavity is a dynamic region characterised by high vortical activity and the presence

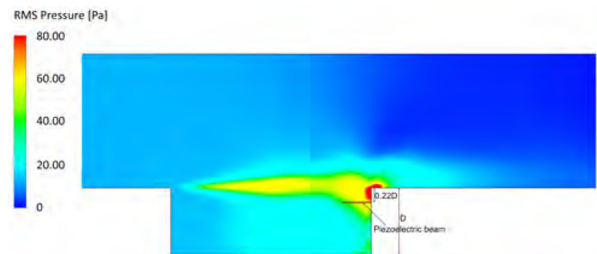


Figure 13. Aft wall location of the piezoelectric beam for CM3 superposed with RMS pressure contour.

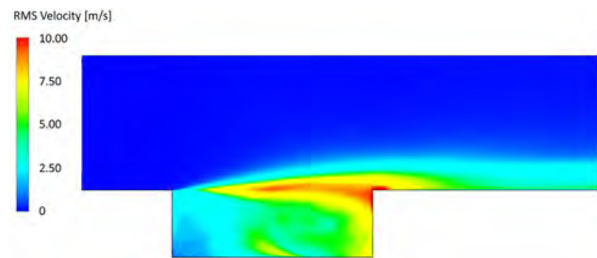


Figure 14. RMS velocity contour for CM3 at mid-plane.

of coherent structures. The Q-criterion vortex identification method by Hunt et al. (1988) is used to reduce the vortical structures that develop in the cavity. The regions of the vortex are defined by the second invariant of the velocity gradient tensor $Q = -1/2(S_{ij}S_{ij} - \Omega_{ij}\Omega_{ij})$ where S and Ω are the strain-rate tensor and the vorticity tensor of the velocity gradient ∇v , respectively. Figure 15 shows the instantaneous vortical structures with iso-surface $Q = 100(U_\infty/L)^2$. It can be observed that cylindrical vortices evolve from the leading edge and grow into larger and stronger hairpin vortices as they reach the trailing edge. The growth and strengthening of these structures would explain the higher levels of floor noise

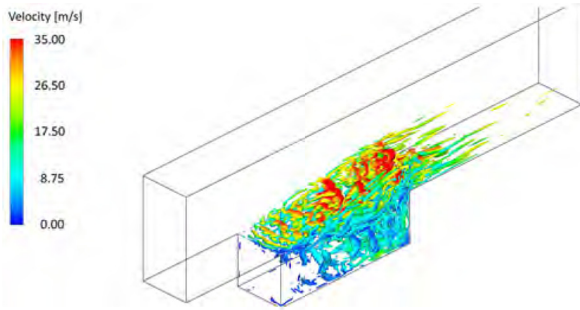


Figure 15. Iso-surfaces of Q criterion.

observed in the spectra at the aft wall (Figure 10). This again points to the aft wall as the ideal location for placement of the energy harvester. For comparative purposes, the corresponding location at the front wall of the cavity was also tested with the energy harvester.

5.3. Piezoelectric beam in cavity

To maximize the energy harvested by the piezoelectric beam, it would be judicious to tune the natural frequency of the piezoelectric beam to match closely and 'lock-in' with the cavity oscillation frequencies, in order to achieve high amplitudes. The tuned natural frequency of the piezoelectric beam is denoted as f_b

hereafter. Four different values of f_b were tested that correspond to f_2 of CM2 and f_1 , f_2 and f_3 of CM3. Tuning of the piezoelectric beam natural frequency was done by adjusting the clamping location and/or by adding tip mass on the cantilever beam. However, before the energy harvesting tests were done, the effect of introducing the piezoelectric beam into the cavity was also considered. The consequences of introducing the piezoelectric beam into the cavity have been studied by comparing the power spectral densities with and without it (baseline case). Figure 16 shows the effect of placing a beam of different f_b values, both at the aft wall as well as the front wall, on the cavity frequency spectrum. For CM2, a slight reduction ($\approx 6\%$) of the dominant cavity frequency, f_2 , was noticed when the piezoelectric beam was located at the aft wall. It can also be noticed that f_1 is more pronounced at the aft wall in this condition. However, when the piezoelectric beam was placed at the front wall, the deviation in f_2 was reduced to 1.5%. For both cases, an increase in amplitude can also be noticed with the introduction of the piezoelectric beam.

For CM3, with the introduction of the piezoelectric beam at the aft wall, an appreciable change of 8.2% in frequency value was noticed for f_2 , similar to CM2. Change in frequency for f_2 , however, was small when the beam was placed at the front wall. A slight increase in the amplitudes of the tones was also noticed with the beam placement. The effects shown in Figure 16 were

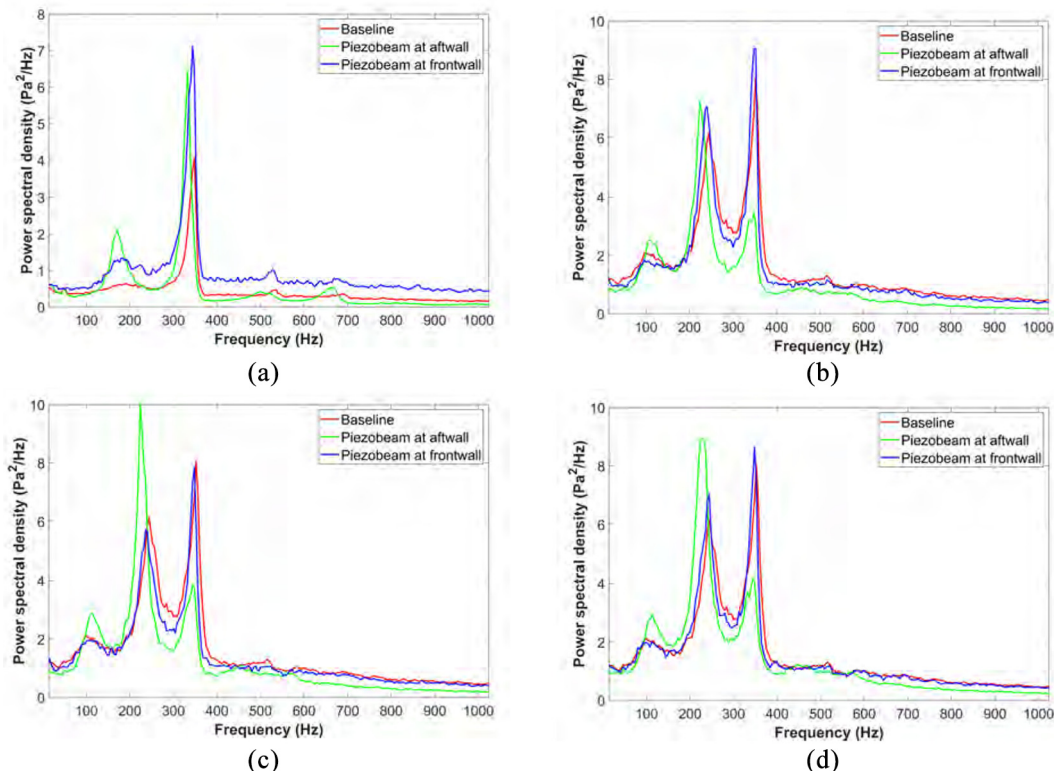
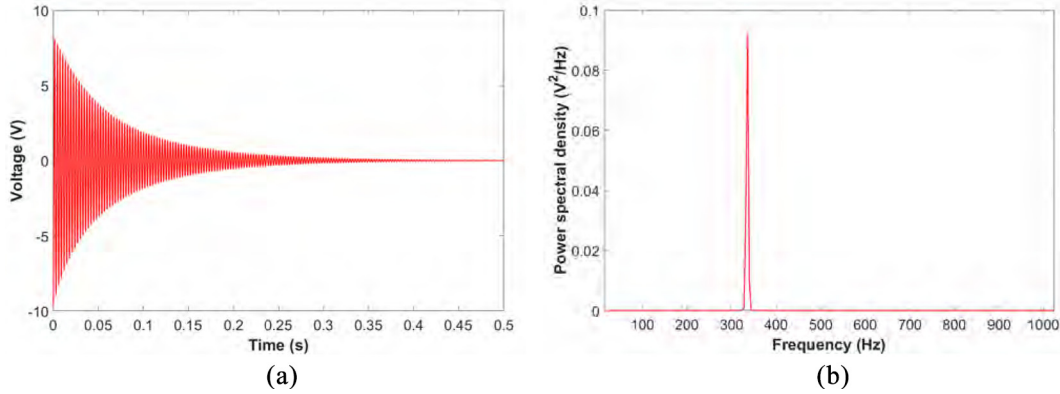


Figure 16. Effect of placing the piezoelectric beam on the cavity oscillation frequencies: (a) $f_b = 332$ Hz ($\approx f_2$ of CM2), (b) $f_b = 108$ Hz ($\approx f_1$ of CM3), (c) $f_b = 228$ Hz ($\approx f_2$ of CM3) and (d) $f_b = 356$ Hz ($\approx f_3$ of CM3).

Table 2. Variation of cavity oscillation frequencies with insertion of piezoelectric beam.

Cavity model	CM2	CM3		
Mode	f_2	f_1	f_2	f_3
Baseline frequency (Hz)	348	116	244	352
Frequency with beam at front wall (Hz)	344	112	240	352
Frequency with beam at aft wall (Hz)	332	108	224	348
Tuned-beam frequency (Hz)	332	108	228	356

**Figure 17.** Voltage output and the corresponding power spectral density of a typical ring out test on the piezoelectric beam: (a) damping of the voltage signal when beam vibrates freely after release and (b) corresponding power spectral density showing the damped natural frequency.

also observed for the microphone data from the front wall and the cavity floor. The change in frequencies induced by placing the beam is most likely due to the beam interfering with the feedback loop and modifying the different time components of it. It has a more significant effect when placed at the aft wall where the shear layer interaction and acoustic pulse generation occurs. As such, the region around the trailing edge is bound to be more sensitive as it is the most dynamic region of the cavity flow oscillation as was witnessed in the CFD results.

The change in the different mode frequencies against the tuning frequency of the piezoelectric beam has been tabulated in Table 2. Three beam natural frequencies (108 Hz, 228 Hz and 332 Hz) were tested for CM3 to match with f_1 , f_2 and f_3 respectively. For CM2, only one beam natural frequency (332 Hz) was tested to match the dominant mode of oscillation, f_2 . The beam length was adjusted to change the frequency between $f_b = 228, 332$ and 356 Hz. To switch f_b to 108 Hz, an additional tip mass was added to the beam condition at $f_b = 228$ Hz. The change in length and addition of tip mass was found to have minimal effect on the cavity frequencies, f_m , for the range considered in the current study. This can be evidenced from Figure 16(b) to (d)

where the cavity flow spectrum shows no change in cavity frequencies with the change in f_b .

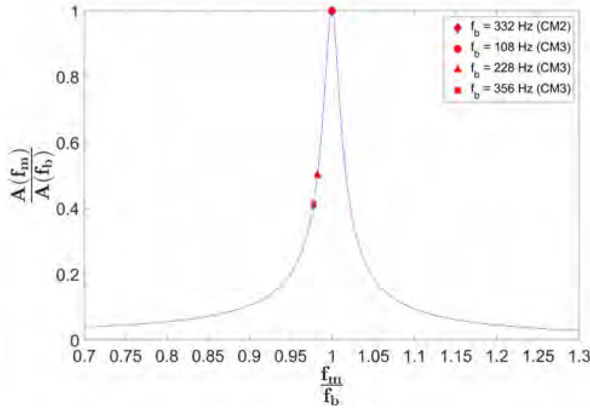
Changing the clamping location of the beam (refer Figure 4) alters the resonating length of the beam, thus varying its resonant frequency. The natural frequency of the beam, f_b , can be estimated from equation (10) as

$$f_b = \frac{0.16 t_b}{L_b^2} \sqrt{\frac{Y_{11}}{\rho_b}} \quad (10)$$

where t_b is the thickness of the piezoelectric film, L_b is the oscillating beam length, Y is the Young's modulus and ρ_b is the density of the beam material. Once the beam was clamped at a given location, the damped natural frequency was measured by deflecting the tip of the beam to 1.5 mm and releasing it to undergo free oscillations. The open-circuit voltage during the free vibrations of such a ring out test was measured, and the power spectral density plotted to determine the damped natural frequency. A typical signal obtained for the damped vibration of the freely oscillating beam is shown in Figure 17 along with the corresponding power spectral density. The free response of the beam depends on the damping ratio, $\zeta = \frac{c}{4\pi m_b f_b}$, where c is the

Table 3. Variation of open circuit V_{RMS} (when released freely from 1.5 mm tip deflection) and $\frac{A(f_m)}{A(f_b)}$ at different values of f_b .

Cavity model	CM2	CM3		
Mode	f_2	f_1	f_2	f_3
f_m (Hz)	332	108	224	348
f_b (Hz)	332	108	228	356
Open circuit V_{RMS} (V)	1.45	2.23	1.54	1.41
$\frac{A(f_m)}{A(f_b)}$	1	1	0.50	0.41

**Figure 18.** Effect of deviation of f_b from f_m on vibration amplitude ($\zeta = .01$).

damping coefficient and m_b is the effective mass of the beam. The damping ratio of the beam oscillation was found to be very small for the cases ($\zeta \approx .01$, estimated using average logarithmic decrement of amplitude) and hence the damped natural frequency obtained from the ring out tests were approximately equal to the natural frequency of the beam.

Resonance of the beam will be achieved when $f_m = f_b$. However, tuning the beam to the exact cavity oscillation frequency is difficult due to the sensitivity of the beam to its length. From equation (10),

$$\frac{df_b}{dL_b} \propto -\frac{1}{L_b^3} \quad (11)$$

which implies that the tuning frequency is very sensitive to the clamping location. The f_b value closest achievable to the cavity oscillation frequencies from Table 2 were thus chosen. The comparison of power generated at different natural frequencies of the beam would not be like-for-like since the response of the beam itself at the different conditions would vary and the departure from resonance ($\Delta f = f_b - f_m$) is also different. The first effect viz. the response of the beam at different conditions to a given excitation can be seen in Table 3. The RMS voltage for the open circuit when the beam is released from a position of 1.5 mm is shown. It can be seen that the beam shows the highest response when

$f_b = 108$ Hz, followed by 228, 332 and 348 Hz respectively. To assess the second effect, equation (13) can be used. For a beam vibration described by equation (13), the ratio of amplitude when forced at cavity oscillation frequency, $A(f_m)$ to amplitude when forced at the resonant condition at its natural frequency, $A(f_b)$, is given as

$$\frac{A(f_m)}{A(f_b)} = \frac{2\zeta}{\sqrt{\left[1 - \left(\frac{f_m}{f_b}\right)^2\right]^2 + \left(2\zeta\frac{f_m}{f_b}\right)^2}} \quad (12)$$

The values of $\frac{A(f_m)}{A(f_b)}$ calculated for the different tuning frequencies that were tested, are shown in Figure 18 and presented in Table 3. Despite the effects of differential response based on f_b and Δf , it was still decided to test three different values of f_b close to $f_m = f_1, f_2$ and f_3 for CM3. This was to observe the energy harvesting capabilities and flow behaviour, when locked in with the different cavity modes. In any given case, the tuned frequency was set to be within ± 8 Hz of the cavity frequency to achieve lock-in effect.

Assuming a single degree-of-freedom for vibrations, the piezoelectric beam under the influence of periodic forcing from the cavity flow field undergoes displacement that can be described (Zhao et al., 2013) by equations (13) and (14) as

$$m_b \frac{d^2 y_b}{dt^2} + c \frac{dy_b}{dt} + k y_b - \theta v = \frac{1}{2} \rho_\infty U_\infty^2 W_b L_b C_y'(t) \quad (13)$$

$$\theta \frac{dy_b}{dt} + C_{pz} \frac{dv}{dt} + \frac{v}{R} = 0 \quad (14)$$

where y_b is the tip displacement of the beam and k is the stiffness of the cantilever beam. θ is the electromechanical coupling coefficient of the beam, v is the continuous voltage signal across the load resistance, C_{pz} is the piezoelectric capacitance and $C_y'(t)$ is the effective exciting force coefficient in the y -direction caused due to cavity flow oscillation. W_b and L_b denote the width and length of the piezoelectric beam respectively. Equation (13) represents the mechanical oscillation of the beam while equation (14) describes the piezoelectric harvester circuit. If the energy harvester circuit is open,

then the resistance value $R \rightarrow \infty$ and equation (14) simplifies to

$$v_{oc} = -\frac{\theta}{C_{pz}} y_b \quad (15)$$

where v_{oc} is the open-circuit voltage. The force coefficient in the y -direction for the current case is due to a combination of pressure forces acting normal to the surface and shear stresses acting tangentially. The effect of shear stresses in the y -direction is relatively insignificant when compared to the pressure forces and can be neglected. Following Figure 19, where $C_p(x', t)$ describes the pressure-coefficient distribution around the piezoelectric beam for a given instant t , the net vertical force coefficient, $C_y(t)$, generated on the beam can be evaluated by integrating the pressure force as

$$C_y(t) = -\oint_{\lambda} C_p(x', t) dx' \quad (16)$$

where λ denotes the closed-curve around the beam surface. x' is the non-dimensional axial co-ordinate shifted from the system origin to the tip of the piezoelectric beam so that $x' = \frac{x-(L-L_b)}{L_b}$. The pressure distribution $C_p(x', t)$ is a periodic function as evidenced in the fluctuating pressure (p') measurement done using microphones. Determining a suitable expression for $C_p(x', t)$ is complicated owing to the nature of the cavity dynamics and flow-structure interaction. However, an approximate expression can be obtained if data is gathered from numerous simulations emulating the flow conditions. Obtaining this would enable the prediction of power generated by the harvester in a cavity flow environment.

5.4. Power generation

The power harvested was estimated by measuring the voltage across the resistor load. The voltage signal across the resistor load was acquired at the same sampling speed as that of the microphone signal. From a given discrete voltage signal (v_i), the RMS voltage (V_{RMS}) and average power (P_{av}) was estimated using equations (17) and (18) as

$$V_{RMS} = \sqrt{\sum_{i=1}^N \left(\frac{v_i^2}{N} \right)} \quad (17)$$

$$P_{av} = \frac{(V_{RMS})^2}{R} \quad (18)$$

The comparison of power spectral densities between the microphone signals at the aft wall and the corresponding piezoelectric beam (located at aft wall) voltage signal during the energy harvesting tests, is shown in Figure 20. The amplitudes have been normalised by

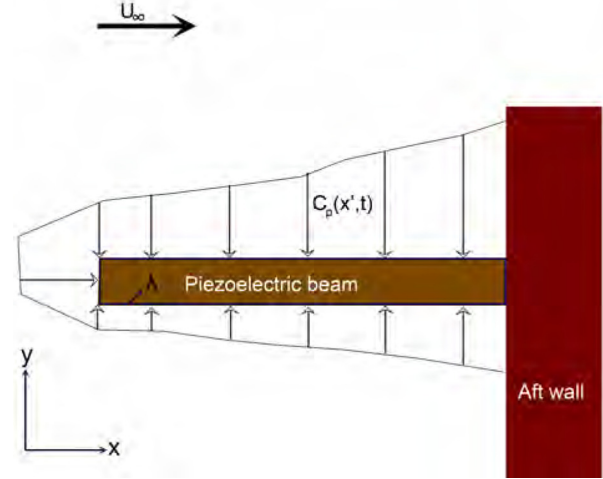


Figure 19. C_p distribution on the piezoelectric beam surface.

maximum value to juxtapose the two spectra for comparison.

The instantaneous power generated was estimated by measuring the voltage across a load resistance abridding the piezoelectric beam terminals. Since the power generated varies with the load, a range of load resistance values were used to determine the optimal resistive load for a given piezoelectric beam setting. The average power variation for CM2 when the beam was tuned to 332 Hz natural frequency is shown in Figure 21(a). The maximum average power was recorded when the beam was located at the aft wall and was $21.1 \mu W$ whereas it fell to $1.87 \mu W$ when located at the front wall. The maximum power for this resonant value occurred at a load resistance value of 10 k Ω . The open-circuit RMS voltages measured for the former and latter cases were 720 and 140 mV, respectively. The maximum peak voltage recorded was 1.68 V, with the corresponding peak instantaneous power of 0.28 mW.

Coherence between the signals obtained from the piezoelectric beam and microphone throws light on how the beam and flow interact at different frequencies. For this, the magnitude-squared coherence, $C_{xy}(f)$, is calculated between the power spectral densities $P_{xx}(f)$ and $P_{yy}(f)$ obtained from the microphone signal (x) and piezoelectric beam (y) as

$$C_{xy}(f) = \frac{|P_{xy}(f)|^2}{P_{xx}(f)P_{yy}(f)} \quad (19)$$

where $P_{xy}(f)$ is the cross power spectral density between x and y . The magnitude-squared coherence values vary between 0 and 1.

Figure 22(a) shows the coherence thus plotted between the microphone signals at the front wall and aft wall of CM2 versus the piezoelectric beam placed at the aft wall. It can be noticed that the coherence value between the aft wall microphone and the beam is

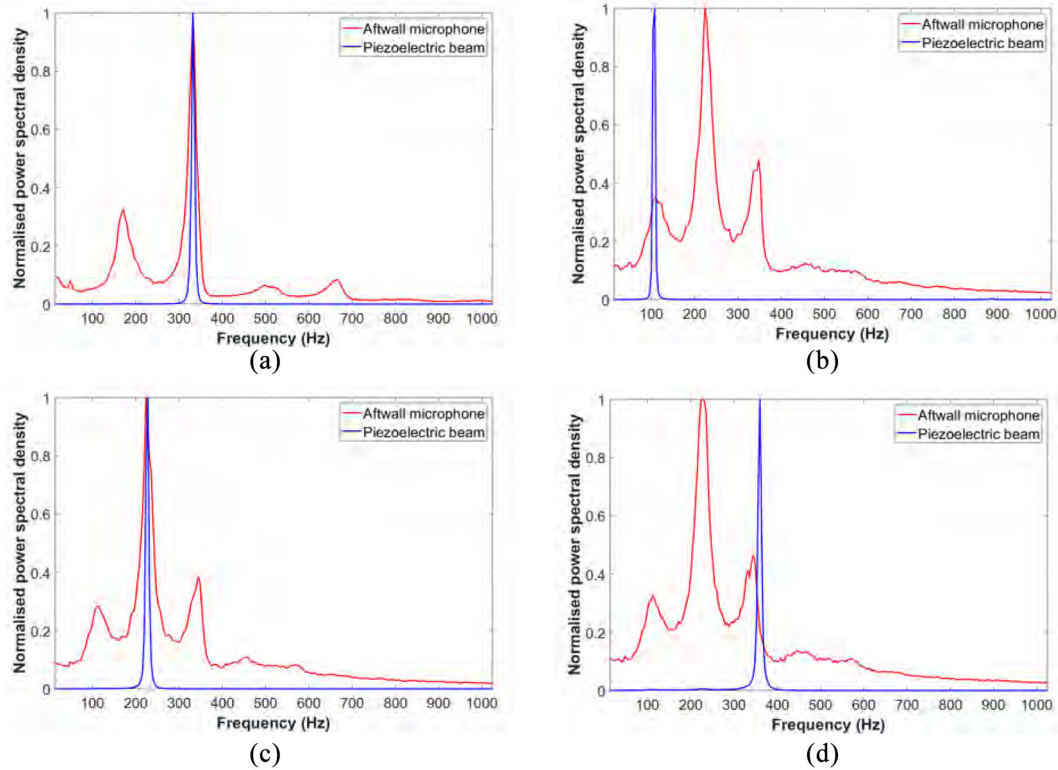


Figure 20. Comparison of normalised power spectra of aft wall microphone signal and piezoelectric beam located at aft wall: (a) lock in between beam and cavity mode f_2 of CM2, (b) lock in between beam and cavity mode f_1 of CM3, (c) lock in between beam and cavity mode f_2 of CM3 and (d) lock in between beam and cavity mode f_3 of CM3.

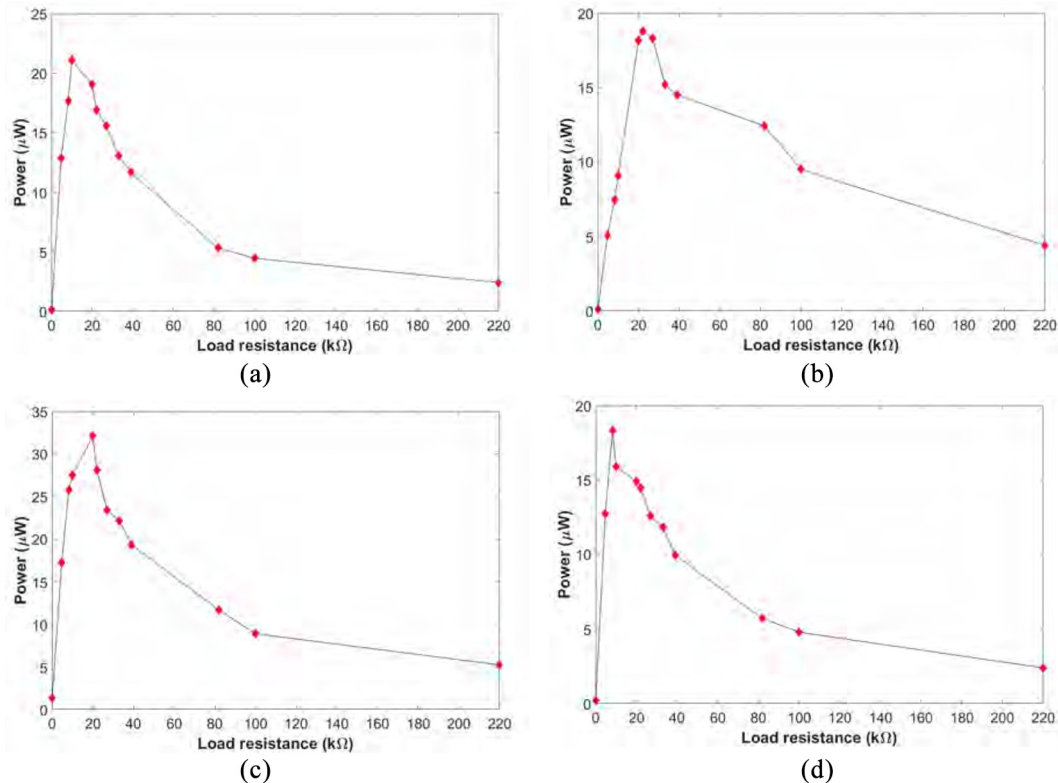


Figure 21. Average power generated by the piezoelectric beam at aft wall for various natural frequencies: (a) beam natural frequency = 332 Hz (CM2), (b) beam natural frequency = 108 Hz (CM3), (c) beam natural frequency = 228 Hz (CM3) and (d) beam natural frequency = 356 Hz (CM3).

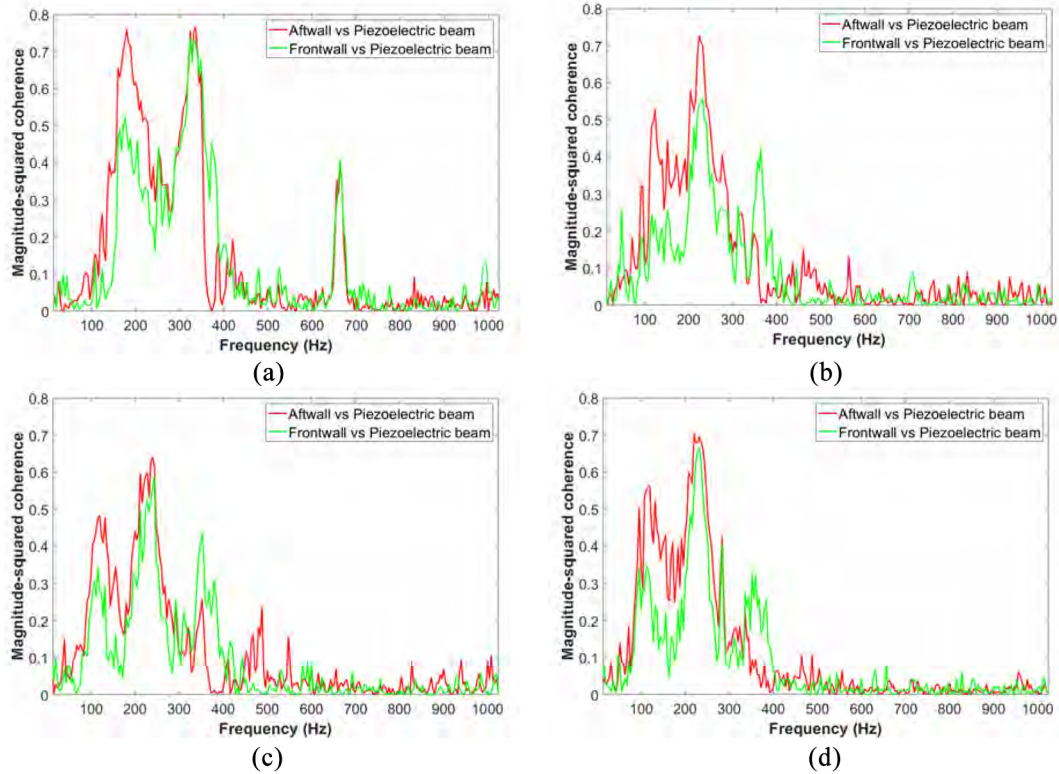


Figure 22. Magnitude squared coherence between signals from microphone and piezoelectric beam: (a) beam at 332 Hz versus microphone signals (CM2), (b) beam at 108 Hz versus microphone signals (CM3), (c) beam at 228 Hz versus microphone signals (CM3) and (d) beam at 356 Hz versus microphone signals (CM3).

almost equal for both f_1 and f_2 which implies the strong coupling of the cantilever beam at these frequencies by the flow. Apart from these, there is also a peak occurring at 664 Hz, which corresponds to the fourth cavity mode. The natural frequency of the beam, 332 Hz, matches with the cavity's second mode f_2 and hence the amplitude of oscillations for the piezoelectric beam is very high at this frequency. However, in the 10-s duration for which the signals were captured, f_1 and f_2 do not co-occur energetically. These two modes compete, and the phenomenon of mode switching is present. This can be seen from the wavelet analysis of the signal obtained from the microphone at the aft wall. Wavelet analysis is a useful tool to study the spectral behaviour of a signal in the time plane with no compromise in the frequency resolution or time resolution as in spectrograms. In the current analysis, a complex Morlet wavelet defined by equation (20) was used as the mother wavelet.

$$\psi_0(x) = \frac{1}{\sqrt{\pi f_{bw}}} \cdot e^{2i\pi f_c t} e^{-\frac{x^2}{f_{bw}^2}} \quad (20)$$

where f_{bw} is a bandwidth parameter and f_c is the wavelet centre frequency. A complex Morlet wavelet with bandwidth parameter 1 and wavelet centre frequency 1.5 Hz

has been used for the current analysis. The scales can be related to frequencies using equation (21).

$$f = \frac{f_c}{a\Delta} \quad (21)$$

where f_c is the wavelet centre frequency, a is the scale and Δ is the sampling period. The scales were chosen from 70 to 614 with a uniform increment of 0.1. In the Continuous Wavelet Transform (CWT), the complex Morlet wavelet is applied as a bandpass filter to the time series. Here the scales chosen restrict the frequencies in the range of 80–700 Hz which encapsulates well all the first three modes. Figure 23(a) shows the contour of wavelet coefficients obtained from the aft wall microphone signal that has been normalized by the maximum absolute value. The signal is shown only for the duration of 0-1 s for clarity. It can be observed from Figure 23(a) that f_2 is present for a prolonged duration of the measurement time with peak amplitudes occurring regularly. f_1 is present only intermittently and can be seen at high amplitudes at sporadic instances, for example when $t = 0.37$ s. It can also be noticed that both f_1 and f_2 do not coexist with high amplitudes. When the amplitude of f_1 has a high magnitude, f_2 can be seen to be weaker and vice versa. This

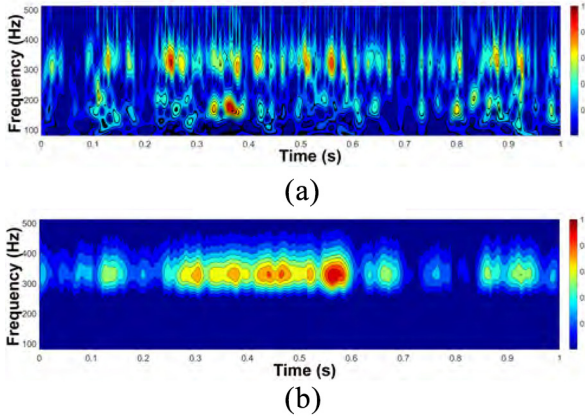


Figure 23. Normalized wavelet coefficients of signals from aft wall microphone and piezoelectric beam (at natural frequency = 332 Hz) for CM2: (a) aft wall microphone and (b) piezoelectric beam at aft wall.

observation has also been noted in a few other works on cavity flows (Kegerise et al., 2004; Vikramaditya and Kurian, 2013; Thangamani, 2019). This explains the relatively low value of f_1 seen in the power spectral density plot since the cavity oscillates at mode 1 only for a short duration of time episodically when compared to f_1 . Comparing the Figure 23(a) and (b) for the time-frequency variation of the signal from the aft wall

microphone and piezoelectric beam, it can be seen that high amplitude oscillations of the beam co-occurs and corresponds to that of f_2 of the acoustic pressure. For example when strong oscillations for f_2 occurs at $t \approx 0.56$ s, strong oscillations can be noticed for the beam as well in Figure 23(b). A saddle region occurs at the resonant frequency of the beam at $t \approx 0.2$ s when f_1 is inconspicuous. It can be inferred that when f_2 dominates the cavity flow oscillations, the beam is forced at its resonant frequency in this case and shows very high amplitudes. When the cavity oscillation mode switches to f_1 , the beam is forced at an off-resonant frequency leading to a low amplitude response from it.

For CM3, three different values of f_b were tested viz. 108, 228 and 356 Hz. These frequencies correspond to f_1, f_2 and f_3 of CM3. As with CM2, high coherence values between the cavity flow oscillations and beam can be noticed in Figure 22(b) to (d). When the beam was tuned to 228 Hz, the dominant mode of oscillation for CM3 with the beam installed, peak average powers of 32.16 and 0.48 μW were recorded when located at aft wall and front wall respectively. The maximum instantaneous voltage and power, in this case, was 2.6 V and 0.3 mW respectively. Figure 24 show the variation of the voltage signal (v_i) and instantaneous power (P_{ins}) over the measurement time for this case. Spikes in the voltage occur when the resonance condition occurs and

Table 4. Average power (P_{av}) and maximum instantaneous power (P_{ins}) when piezoelectric beam is located at front and aft wall at different tuned lock-in frequencies.

Cavity model	CM2	CM3		
Tuned beam-frequency (Hz)	332	108	228	356
	($\approx f_2$)	($\approx f_1$)	($\approx f_2$)	($\approx f_3$)
P_{av} in μW (front wall)	1.87	1.32	0.48	0.41
Max. P_{ins} in μW (front wall)	30.43	14.59	8.95	7.02
P_{av} in μW (aft wall)	21.11	18.81	32.16	18.31
Max. P_{ins} in μW (aft wall)	284.18	304.84	339.42	403.46

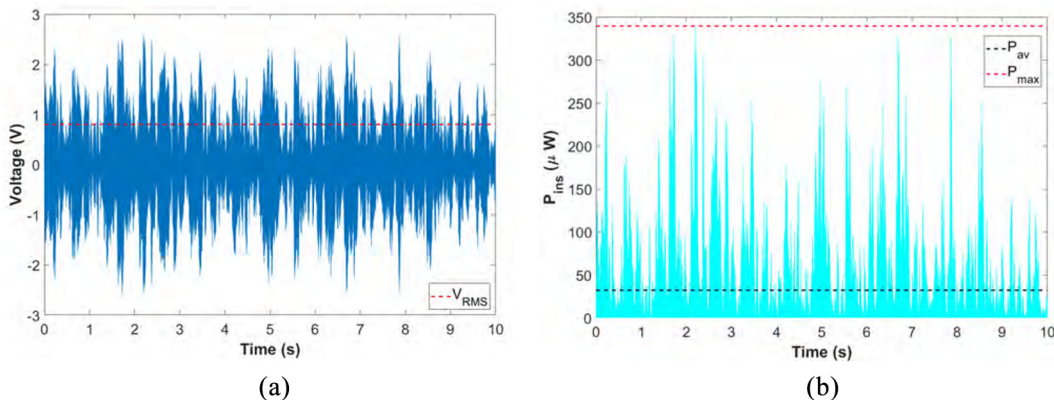


Figure 24. Variation of instantaneous voltage and power across the measurement time for CM3 when $f_b = 228$ Hz: (a) instantaneous voltage variation and (b) instantaneous power variation.

the cavity has the dominant mode of oscillation at f_2 . This phenomenon was noticed for CM2 as well, discussed before and shown in Figure 23. For the case when the beam was tuned to 356 Hz, the peak powers recorded were 18.31 and 0.41 μW for the beam location at the aft wall and front wall respectively. Similar to the time-frequency discussion for CM2, here also the beam is excited to very high amplitudes when the cavity oscillations are near the resonant frequency. Average and peak instantaneous power of 18.81 μW and 304.81 μW was measured when $f_b = 108$ Hz. Given the low amplitude of f_1 seen in Figure 16(b), the power is still comparable with the dominant frequencies. This is because of the strong response of the beam at $f_b = 108$ Hz as described in Table 3. Table 4 shows the average and maximum instantaneous power generated by the piezoelectric beam at various conditions. As expected, the power yielded when the beam is located at the front wall is poor due to the lower levels of pressure fluctuation near the leading edge as compared to the trailing edge.

6. Conclusion

The energy harvesting prospects of cavity flow oscillations were investigated by considering two different cavity geometries of $L/D = 2$ and 3 with an incoming flow of 30 m/s. The frequency spectra of the baseline cavities, obtained using microphones, showed high amplitude frequencies corresponding to Rossiter's model. While the second mode of oscillation dominated for the cavity with $L/D = 2$, both the second and third mode of oscillation co-dominated for the cavity with $L/D = 3$. To harvest the oscillatory energy at these frequencies, a piezoelectric beam was tuned to match its natural frequency with them closely. The piezoelectric beam was located perpendicularly to the aft wall of the cavity at a distance of $0.22D$ from the trailing edge, which was shown by CFD results to be a region of highly fluctuating pressure levels. Average power of 21.11 μW and maximum instantaneous power of 0.28 mW was recorded for the cavity with $L/D = 2$ when the piezoelectric beam was tuned to the dominant frequency. For the cavity with $L/D = 3$, an average power of 32.16 μW and peak power of 0.34 mW was recorded for its dominant mode of oscillation. Coherence study between the fluctuating pressure and the piezoelectric signal showed a high value of coherence at the cavity frequencies. The time-frequency study of the signals using wavelet analysis showed that the cavity modes switched between the different active modes. When the cavity mode switched to the frequency closer to the natural frequency of the piezoelectric beam, high amplitudes of voltage was recorded.

The study highlights the promise that self-sustained cavity flow oscillations hold from an energy harvesting perspective. An additional encouraging factor is the presence of multiple dominant frequencies at which energy can be harvested, as opposed to several other methods employed in harvesting flow-induced vibrations, wherein only a single dominant forcing frequency is available. There also is much scope to improve the energy harvested by this method since in the current study it was seen that the energy harvester was yielding trivial power when the frequency of cavity flow oscillation differed from its natural frequency.

Acknowledgement

We wish to gratefully acknowledge and thank the Government of Malaysia for supporting this work. The authors also acknowledge the use of the IRIDIS High Performance Computing Facility at the University of Southampton, UK, in the completion of this work.


Declaration of conflicting interests

The authors declared no potential conflicts of interest with respect to the research, authorship, and/or publication of this article.

Funding

The authors disclosed receipt of the following financial support for the research, authorship, and/or publication of this article: This research was supported by the Ministry of Higher Education (MoHE), Malaysia, through the Fundamental Research Grant Scheme FRGS/1/2018/TK10/USMC/03/1.

ORCID iD

Varun Thangamani  <https://orcid.org/0000-0003-3515-9540>

References

- Abdelkefi A (2016) Aeroelastic energy harvesting: A review. *International Journal of Engineering Science* 100: 112–135.
- Ahuja KK and Mendoza J (1995) Effects of cavity dimension, boundary layer and temperature on cavity noise with emphasis on benchmark data to validate computational aeroacoustic codes. *Technical Report 4653, Georgia Institute of Technology*. Atlanta, Georgia.
- Akaydin H, Elvin N and Andreopoulos Y (2010a) Energy harvesting from highly unsteady fluid flows using piezoelectric materials. *Journal of Intelligent Material Systems and Structures* 21(13): 1263–1278.
- Akaydin H, Elvin N and Andreopoulos Y (2010b) Wake of a cylinder: A paradigm for energy harvesting with piezoelectric materials. *Experiments in Fluids* 49(1): 291–304.
- Allen J and Smits A (2001) Energy harvesting eel. *Journal of Fluids and Structures* 15(3–4): 629–640.
- Bibo A, Abdelkefi A and Daqaq M (2015) Modeling and characterization of a piezoelectric energy harvester under

- combined aerodynamic and base excitations. *Journal of Vibration and Acoustics, Transactions of the ASME* 137(3): 031017-1–031017-12.
- Bryant M and Garcia E (2011) Modeling and testing of a novel aeroelastic flutter energy harvester. *Journal of Vibrations and Acoustics* 133(1): 011010-1–011010-11.
- Cattafesta L III, Williams D, Rowley C, et al. (2003) Review of active control of flow-induced cavity resonance. In: *33rd AIAA fluid dynamics conference and exhibit, AIAA, Orlando, FL: Florida, 23–26 June 2003*.
- Chang K, Constantinescu G and Park SO (2006) Analysis of the flow and mass transfer processes for the incompressible flow past an open cavity with a laminar and a fully turbulent incoming boundary layer. *Journal of Fluid Mechanics* 561: 113–145.
- Chatellier L, Laumonier J and Gervais Y (2004) Theoretical and experimental investigations of low Mach number turbulent cavity flows. *Experiments in Fluids* 36(5): 728–740.
- Dunnmon J, Stanton S, Mann B, et al. (2011) Power extraction from aeroelastic limit cycle oscillations. *Journal of Fluids and Structures* 27(8): 1182–1198.
- Goushcha O, Akaydin H, Elvin N, et al. (2015) Energy harvesting prospects in turbulent boundary layers by using piezoelectric transduction. *Journal of Fluids and Structures* 54: 823–847.
- Hamlehdar M, Kasaeian A and Safaei M (2019) Energy harvesting from fluid flow using piezoelectrics: A critical review. *Renewable Energy* 143: 1826–1838.
- Hartog J (1985) *Mechanical Vibrations*. New York, NY: Dover publications Inc.
- Heller H and Bliss D (1975) The physical mechanism of flow induced pressure fluctuations in cavities and concepts for their suppression. In: *2nd Aeronautics conference, AIAA paper, AIAA, Hampton, VA: Virginia, 24–26 March 1975*.
- Hunt JCR, Wray AA and Moin P (1988) Eddies, streams, and convergence zones in turbulent flows. Technical Report CTRS88, Center for Turbulence Research. Stanford, CA: California.
- Kegerise M, Spina E, Garg S, et al. (2004) Mode switching and nonlinear effects in compressible flow over a cavity. *Physics of Fluids* 16(3): 678–687.
- Kirkup L and Frenkel RB (2006) *An introduction to uncertainty in measurement: using the GUM (guide to the expression of uncertainty in measurement)*. Cambridge University Press, Cambridge, UK: United Kingdom, pp.97–109.
- Larcheveque L, Sagaut P and Labbé O (2007) Large-eddy simulation of a subsonic cavity flow including asymmetric three-dimensional effects. *Journal of Fluid Mechanics* 577: 105.
- Ma R, Slaboch P and Morris S (2009) Fluid mechanics of the flow excited Helmholtz resonator. *Journal of Fluid Mechanics* 623: 1–26.
- Matova S, Elfrink R, Vullers R, et al. (2011) Harvesting energy from airflow with a micromachined piezoelectric harvester inside a Helmholtz resonator. *Journal of Micromechanics and Microengineering* 21(10): 104001-1–104001-6.
- Mitcheson P, Yeatman E, Rao G, et al. (2008) Energy harvesting from human and machine motion for wireless electronic devices. *Proceedings of the IEEE* 96(9): 1457–1486.
- Rossiter J (1964) Wind tunnel experiments on the flow over rectangular cavities at subsonic and transonic speeds. Technical Report 64037, Ministry of Aviation; Royal Aircraft Establishment, RAE, Farnborough.
- Saddington A, Knowles K and Thangamani V (2016a) Scale effects on the performance of sawtooth spoilers in transonic rectangular cavity flow. *Experiments in Fluids* 57(1): 1–12.
- Saddington A, Thangamani V and Knowles K (2016b) Comparison of passive flow control methods for a cavity in transonic flow. *Journal of Aircraft* 53(5): 1439–1447.
- Sirohi J and Mahadik R (2011) Piezoelectric wind energy harvester for low-power sensors. *Journal of Intelligent Material Systems and Structures* 22(18): 2215–2228.
- Smagorinsky J (1963) General circulation experiments with the primitive equations: I. The basic experiment. *Monthly Weather Review* 91(3): 99–164.
- Thangamani V (2019) Mode behavior in supersonic cavity flows. *AIAA Journal* 57(8): 3410–3421.
- Thangamani V, Knowles K and Saddington A (2014) Effects of scaling on high subsonic cavity flow oscillations and control. *Journal of Aircraft* 51(2): 424–433.
- Thangamani V and Kurian J (2013) Control of cavity oscillations in a supersonic flow by microjet injection. *Journal of Aircraft* 50(4): 1305–1308. DOI:10.2514/1.C032003.
- Tracy MB and Plentovich EB (1993) Characterization of cavity flow fields using pressure data obtained in the Langley 0.3-meter transonic cryogenic tunnel. *Technical Report 4436, NASA*. Hampton, VA: Virginia.
- Verdugo F, Guitton A and Camussi R (2012) Experimental investigation of a cylindrical cavity in a low Mach number flow. *Journal of Fluids and Structures* 28: 1–19.
- Vikramaditya N and Kurian J (2013) Amplitude and phase modulation of cavity modes in a supersonic flow. *European Journal of Mechanics, B/Fluids* 42: 159–168.
- Wen Q, Schulze R, Billep D, Otto T, et al. (2014) Modeling and optimization of a vortex induced vibration fluid kinetic energy harvester. *Procedia Engineering* 87: 779–782.
- Zhang X, Rona A and Edwards J (1998) An observation of pressure waves around a shallow cavity. *Journal of Sound and Vibration* 214(4): 771–778.
- Zhao L, Tang L and Yang Y (2013) Comparison of modeling methods and parametric study for a piezoelectric wind energy harvester. *Smart Materials and Structures* 22(12): 125003-1–125003-12.
- Zou H, Chen H and Zhu X (2015) Piezoelectric energy harvesting from vibrations induced by jet-resonator system. *Mechatronics* 26: 29–35.

Appendix I

Notation

α	phase constant between downstream propagating vortical disturbance and upstream propagating acoustic wave
δ^*	displacement thickness of boundary layer
δ_{99}	boundary layer thickness based on 99% freestream velocity
δ_{ij}	Kronecker delta
$\epsilon_{0.95}$	standard error based on 95% confidence interval
ν	dynamic viscosity
ν_{SGS}	subgrid scale viscosity

\bar{p}	time-averaged pressure	P_{ins}	instantaneous power harvested
$\phi_0(x)$	complex Morlet wavelet function	$P_{xx}(f)$	power spectral density of signal x
ρ	fluid density	$P_{xy}(f)$	cross power spectral density between signals x and y
ρ_b	density of piezoelectric beam material	$P_{yy}(f)$	power spectral density of signal y
σ	standard deviation	S_{ij}	subgrid scale shear strain tensor
τ_{ij}	subgrid scale stress	t_b	thickness of piezoelectric beam
θ	momentum thickness of boundary layer	u'_i	filtered velocity component
Δ	LES filter width	U_∞	freestream velocity
ζ	damping ratio	v	voltage across resistor load
C_s	Smagorinsky constant	v_i	instantaneous voltage
$C_{xy}(f)$	magnitude-squared coherence between signals x and y	V_{RMS}	RMS voltage
d_{31}, d_{33}	piezoelectric charge coefficients	y^+	non-dimensional wall normal distance
f_1, f_2, f_3	frequency of first, second and third modes of cavity flow oscillation	Y_{11}, Y_{33}	Young's modulus of elasticity
f_c	wavelet centre frequency	a	wavelet scale
f_m	frequency of m^{th} mode of cavity flow oscillation	CFL	Courant number
f_{bw}	bandwidth parameter in mother wavelet	CM2	cavity model with $L/D = 2$
f_b	natural frequency of piezoelectric beam	CM3	cavity model with $L/D = 3$
g_{31}, g_{33}	piezoelectric voltage coefficients	D	depth of rectangular cavity
k	ratio of freestream velocity to vortex convection velocity	L	length of rectangular cavity
k_{31}, k_{33}	piezoelectric coupling coefficients	m	cavity oscillation mode number
L_b	length of piezoelectric beam	PZT	lead zirconate titanate
M_∞	freestream Mach number	Q	velocity gradient tensor
p'	fluctuating pressure	RMS	root mean square
p_i	instantaneous pressure	t	time
P_{av}	average power harvested	u'	fluctuating velocity in the x -direction
		v'	fluctuating velocity in the y -direction
		W	width of rectangular cavity